

Comprehensive characterization of ligand unbinding mechanisms and kinetics for T4 lysozyme mutants using τ RAMD

Ariane Nunes-Alves^{a,b}, Daria B. Kokh^a, Rebecca C. Wade^{a,b,c}*

^aMolecular and Cellular Modeling Group, Heidelberg Institute for Theoretical Studies, Schloss-Wolfsbrunnenweg 35, 69118 Heidelberg, Germany

^bCenter for Molecular Biology (ZMBH), DKFZ-ZMBH Alliance, Heidelberg University, Im Neuenheimer Feld 282, 69120 Heidelberg, Germany

^cInterdisciplinary Center for Scientific Computing (IWR), Heidelberg University, Im Neuenheimer Feld 205, Heidelberg, Germany.

Corresponding Author: Rebecca.Wade@h-its.org

ANA and DBK are joint first authors.

Abstract:

The computation of dissociation rates from modeling of macromolecule-ligand unbinding processes is a topic of recent and increasing interest for drug design applications. However, the complexity of the high-dimensional space explored during dissociation on timescales that often exceed those accessible to conventional molecular dynamics (MD) simulations make this task highly challenging. Introduction of a scaling potential or additional force can accelerate the dissociation process, but may affect the reliability of simulated egress paths and thus observed mechanisms and computed residence times. We address this problem by exploring the dissociation of benzene and indole from T4 lysozyme mutants. We employ the τ -Random Acceleration Molecular Dynamics (τ RAMD) method, in which a small randomly oriented force is applied to the ligand to facilitate its unbinding during MD simulations. We find that τ RAMD yields the ranking of dissociation rates for the simulated ligands, protein mutants and temperature conditions in good accordance with experiments. Comparison of the unbinding paths and metastable states of benzene from the L99A mutant reveals a good agreement of τ RAMD with much more computationally demanding conventional MD simulations. Moreover, mapping of the egress routes for all the systems studied shows that visiting more metastable states slows dissociation and indicates that accurate dissociation rates can be computed without exhaustive sampling, as long as the main egress route is sampled. Overall, this study provides physical insights that could be exploited in the rational optimization of the kinetic properties of drug candidates.

Main Text

Introduction

The residence time of a ligand-protein complex (τ , given by the inverse of the dissociation rate: $1/k_{\text{off}}$) is a kinetic parameter defining the time required for dissociation of a bound complex, which in turn directly affects the concentration of the bound protein under both equilibrium and non-equilibrium conditions^{1,2}. τ has become an important parameter in drug design, since it has been increasingly reported that drug efficacy is better correlated with τ than with the binding affinity of a drug-target complex^{3,4}. This has stimulated the development of computational methods to predict residence times. One of the main challenges in the prediction of τ is the timescales involved. Although simulations of protein systems may now routinely extend to microseconds, they are short compared to typical values of τ for drug-like molecules. To overcome this problem, many computational methods to enhance sampling of ligand unbinding during MD simulations have been proposed^{5,6}. One group of methods aims at computing absolute values of τ by correcting from the enhanced sampling system back to the original statistical ensemble. This group includes methods such as weighted ensemble MD⁷, in which trajectories occupying bins along a progress coordinate are split and merged, and metadynamics^{8,9}, in which the potential energy of the system is adjusted. Another group of methods aims at using shorter simulations of perturbed systems in order to compute the relative values of τ for a set of protein-ligand complexes. This group includes methods such as scaled molecular dynamics¹⁰ in which potential energy terms are (completely or in part) scaled down, targeted MD^{11,12} which employs a pulling force on the system along a reaction coordinate, and τ RAMD^{13,14} where a randomly oriented force is applied to the ligand during MD simulations to enhance the rate of ligand unbinding from its initial bound

state. These methods have been shown to be useful for the prediction of τ for drug-like compounds. However, being non-equilibrium by nature, the reliability of these methods is based on the trade-off between computational time and the accuracy of the simulated dynamics of the system. It remains to be determined to what extent methods that change the energy landscape or forces correctly capture mechanistic details, such as metastable states along ligand egress routes.

T4 lysozyme (T4L) mutants that contain engineered small artificial cavities that can accommodate benzene and indole derivatives have long served as model systems for investigating protein-small molecule interactions^{15,16}. Recently, however, these T4L mutants have been the subject of renewed interest because advances in computational techniques indicate the possibility to fully characterize ligand binding and unbinding mechanisms. Consequently, no less than thirteen computational studies have been published since 2018 by different research groups in which methods based on MD simulation were used to identify paths from a buried cavity to the T4L exterior and to try to characterize the ligand binding and unbinding processes energetically and kinetically (see ref⁶ and references^{17,18,27-29,19-26}). A comparative analysis of these results⁶ revealed not only agreement but also discrepancies and limitations in these studies. This prompted us to apply our τ -Random Acceleration Molecular Dynamics (τ RAMD) methodology¹³ to this system in order to assess its ability to rank complexes by τ and to characterize ligand egress routes and reveal ligand dissociation mechanisms.

We first used the τ RAMD approach to compute the relative dissociation rates of benzene from three T4L mutants having the single-point mutations L99A, M102A and F104A (with the corresponding mutants referred to here as T4L L99A, T4L M102A and T4L F104A), and for indole from T4L L99A. The L99A and M102A mutations create solvent inaccessible cavities for ligand

binding in the C-terminal domain of T4L, whereas the F104A mutation creates a solvent accessible crevice for ligand binding. We compared the computed relative dissociation rates with the data obtained from nuclear magnetic resonance (NMR) measurements³⁰ for these complexes at three different temperatures, which yield a good agreement. We therefore went on to assess whether the τ RAMD simulations sample the same pathways as seen previously in MD simulations using different enhanced sampling strategies^{17,21–25} and the same metastable states previously observed in conventional MD simulations for benzene and T4L L99A²⁶. Notably, the latter study provided a rather accurate prediction of the absolute dissociation rate (with a three-fold error factor), despite the fact that it sampled fewer pathways (three) than other computational studies (which sampled from four to eight pathways)^{17,22,23}. To explore the dissociation pathways, we employ a recently developed protocol for the generation and analysis of protein-ligand interaction fingerprints along MD simulations, MD-IFP³¹. The mechanistic insights obtained from the τ RAMD simulations allow us to understand how the presence of metastable states along ligand egress paths can affect residence times and how good estimates of protein-ligand residence times can be obtained without having to sample all the egress paths.

Results and Discussion

τ RAMD accurately predicts relative residence times for benzene and indole bound to T4L mutants

τ RAMD was used to compute relative residence times at 20 °C for indole and benzene bound to T4L L99A, and benzene bound to two additional T4L mutants: T4L M102A and T4L F104A. Additionally, the dissociation of benzene from T4L L99A was simulated at 10 °C and 30 °C to compare with the experimental measurements in Ref.³⁰. The computed relative residence times

are plotted versus experimental data in **Figure 1**. Note that we applied a smaller force (4 kcal/(mol Å)) than in our study of drug-like inhibitors of HSP90¹³ (14 kcal/(mol Å)) to ensure the dissociation of the fragments from T4L on the nanosecond timescale. The standard deviation of the measured τ for T4L F104A is large, which may contribute to the uncertainty of linear fitting of computed versus experimental rates. In general, however, the computed data show a remarkably good correlation with experiment ($R^2 = 0.78$), with an average error of about 38% of the experimental dissociation rate, which is within the uncertainty observed in our study of many inhibitors of HSP90¹³, and was obtained despite the fact that we compare τ values for different protein mutants, different physical conditions (temperatures), and different compounds.

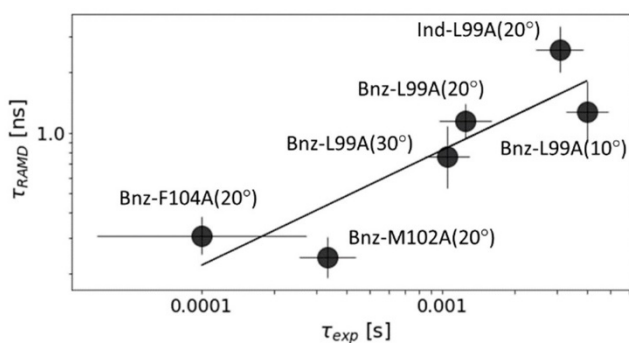


Figure 1. Comparison of computed (τ_{RAMD}) and measured (τ_{exp}) residence times for benzene and indole for three T4L mutants at 10 °C, 20 °C and 30 °C. Values are shown on the logarithmic scale and a linear fitting of computed to experimental data with $R^2=0.78$ is shown by the black line.

The populations of the unbinding paths depend on the binding site, ligand type and temperature

To explore the ligand egress pathways, we identified and analyzed interaction fingerprints (IFPs) for the last 300 snapshots (i.e. 0.3 ns) of each RAMD trajectory, which generally encompass

the last part of the ligand motion in its bound state and the complete ligand unbinding process. The results were similar when the last 500 snapshots of each RAMD trajectory were used (see **Figure S1**). The computed IFP binary vector for each snapshot describes hydrogen bonds, hydrophobic and aromatic contacts between the ligand and all the protein residues along the dissociation trajectories (the vector elements are assigned values of 1/0 depending on whether a specific interaction is detected or not). We specified ligand egress pathways by the last frame in which at least two protein-ligand interactions were still present before complete dissociation. Based on the hierarchical clustering of combined non-zero protein-ligand IFPs obtained from all dissociation trajectories of benzene from T4L L99A (simulated at three different temperatures), a total of five egress routes were identified (see **Figure 2A**): FGH (unbinding through helices F, G and H), DG, HJ, CD and FI. All these pathways were also observed and characterized in previous studies^{17,22,23,26,32,33}. Path CF^{17,19,22,23} was not detected in the present simulations, but it was observed for indole unbinding with a low population (see discussion below and **Figure S2**). Pathway EJ, which was revealed for the first time in metadynamics simulations of ligand binding²² (referred to as H), was not observed here either, likely due to its low population as reported in Ref.²². Furthermore, the egress channel HJ is quite wide (see **Figure S3**) and could be further subdivided as was done in this metadynamics study²².

The predominant dissociation route from T4L L99A and T4L M102A was FGH, although increasing the temperature from 10 to 30 °C slightly reduced egress via FGH in favor of less populated routes, particularly DG (**Figure 2**). These results provide a possible reason why only the FGH route was reported in several previous studies^{28,29,32,33}. Remarkably, despite the strong differences in population, there is only a small difference in the average dissociation times computed for all the pathways, with slightly higher values for lowly populated routes (CD and FI,

see **Figure S3**). This difference is, however, within the uncertainty of the simulated dissociation times. These results agree with other studies, in which similar preliminary kinetic rates¹⁷ or unbinding times²³ were computed for the different paths. Moreover, the fact that path FGH has the highest population explains why a reasonably accurate prediction of the unbinding rate for benzene could be made without exhaustive pathway sampling²⁶. Such predictions can be achieved as long as the main path, FGH, is sampled.

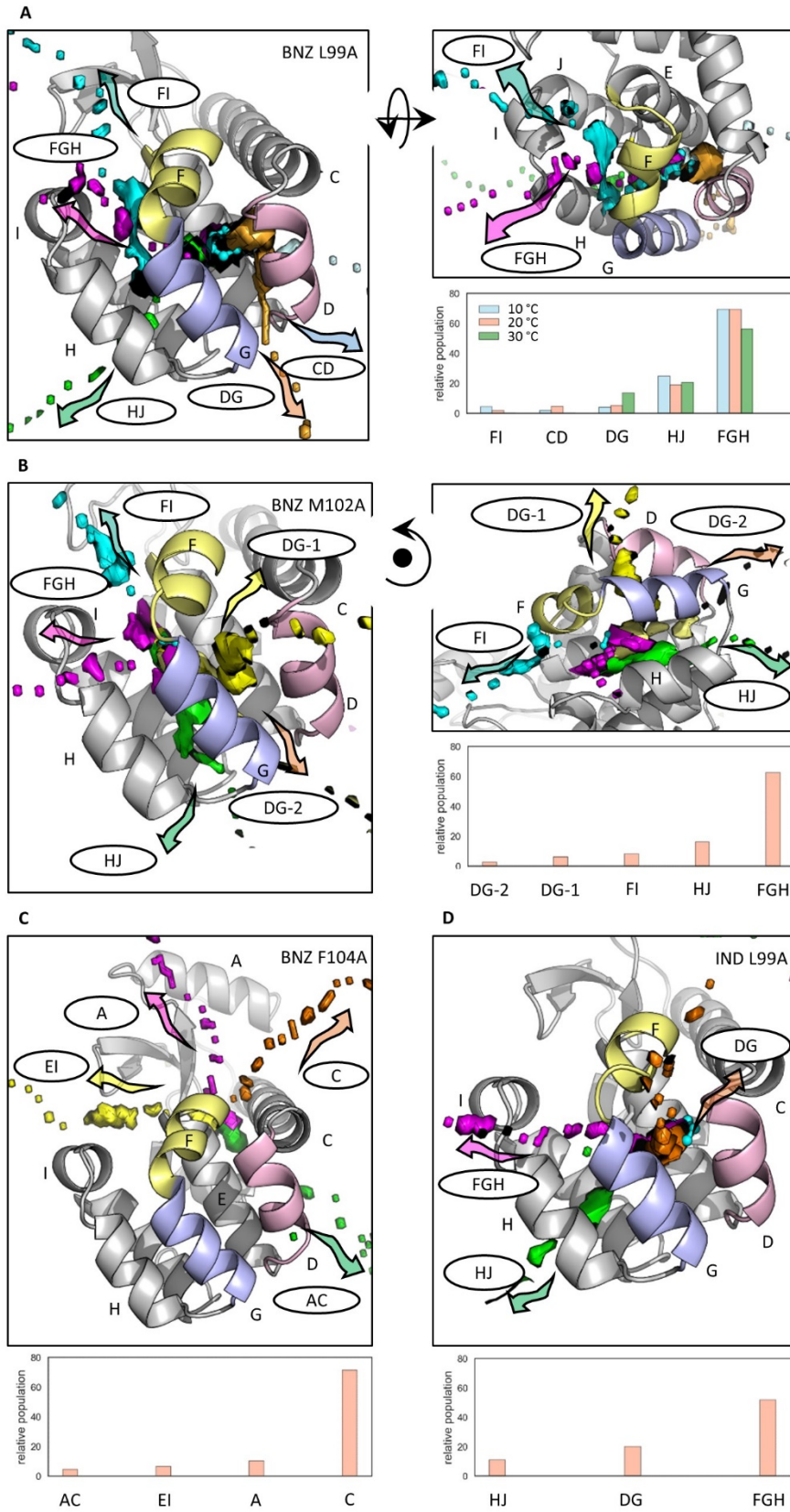


Figure 2. *Paths and their relative populations for benzene dissociation from T4L L99A at 10 °C, 20 °C, and 30 °C (A), benzene dissociation from T4L M102A (B) and T4L F104A (C), and indole dissociation from T4L L99A (D) at 20°C. The main dissociation paths observed were obtained from hierarchical clustering (see main text) and are labeled according to the helices that they pass between. Each path is represented by one or two arbitrarily chosen dissociation trajectories (that belong to the corresponding cluster) displayed as isosurfaces of the population density obtained by mapping positions of the ligand center of mass (COM) in all frames of the trajectory onto a 3D grid. The directions of dissociation are indicated by arrows. The protein is shown in cartoon representation with helices labelled by letters and helices D, F and G colored pink, yellow and blue, respectively. The ligands are shown in cyan ball-and-stick representation in their bound position.*

The bound position of benzene in T4L M102A is slightly shifted towards A102 relative to its position in T4L L99A, while in T4L F104A it occupies another binding site that is large and highly solvent-exposed. Accordingly, the egress routes for benzene dissociation from T4L M102A are very similar to those for T4L L99A: FGH, DG, HJ and FI. In this case, the DG route can be divided into DG-1 and DG-2, depending on whether the dissociation direction is perpendicular or parallel to the D and G helices (**Figures 2B and S4**). The absence of the CD path for this mutant is likely due to the initial position of benzene, which is closer to a metastable state that leads to unbinding through paths FGH and HJ (see further discussion below).

Four main paths were found for benzene from the large open cavity in T4L F104A that is lined by helices A, C and E. Most of these paths lead directly from the cavity, but a few trajectories were also observed in the opposite direction, via pathway AC (see **Figures 2C and S5**).

Finally, the dissociation routes of indole from T4L L99A, from the same bound position as benzene, are quite similar (see **Figures 2D and S6**). However, path CD, which was observed for benzene, had a low population for indole, likely due to its larger size (see **Figure S2**). Path FI was not identified for indole, but could be considered as part of the wider path FGH (see **Figure S6**).

Finally, it is important to note that most of the pathways detected could be subdivided further depending on the threshold applied for hierarchical clustering and the level of resolution of the pathway definition (see **Figures S3-S6**).

Visiting multiple intermediate metastable states makes dissociation slower

Metastable states on the dissociation pathways for each complex were identified using k-means clustering of the complete set of IFPs obtained from the last 300 frames of each dissociation trajectory (see Material and Methods for details). The pattern of the metastable states for the benzene-T4L L99A system is very similar for all three temperatures simulated (**Figures 3A and S7**): there are generally two metastable states with relatively low populations at average RMSD values of about 10 Å (clusters 6 and 7; cluster 8 corresponds to the unbound state), which are intermediates on the dissociation paths FGH and HJ (**Figure 2A**), and there is a highly populated state 5 (i.e. an often visited metastable state) at RMSD ~ 5 Å where benzene is located close to the side-chain of M102. All other states (average RMSD < 3 Å, clusters 1 - 4 in **Figure 3A**) are quite close to the bound state and are interconnected by multiple transitions. The dissociation flow can be described as ligand transitions from metastable state 4 to 5, 6, and then complete dissociation (see gray arrows in **Figure 3A**). Direct transitions from the bound states 1 and 3 to the dissociated

state (via paths CD and DG, respectively) and from 5 to 7 to dissociation (route HJ) are also observed, albeit with a lower probability.

To compare the metastable states observed in the present study with those revealed in several much more computationally extensive simulations of the benzene - T4L L99A system, even though their position was not always exactly characterized relative the protein structure, we considered four studies: (i) 60 μ s of conventional MD trajectories ²⁶, (ii) generalized replica exchange (gREST) simulations ²⁷, (iii) Gaussian accelerated molecular dynamics (GaMD) sampling ³², and (iv) accelerated molecular dynamics (aMD) dissociation trajectories ²⁵.

In the conventional MD simulations of ligand binding accompanied by a Markov State Model analysis, two main intermediate macrostates were identified ²⁶: MS1 between helices G and H and MS2 between helices D and G. Both macrostates are quite diffuse and correspond to rather large distributions of the benzene positions. In particular, MS2 covers the complete region between helices D and G, which is represented by clusters 1-4 close to the bound state in our simulations (see **Figure 3A**). The macrostate MS1, an intermediate on the main association pathway, is even more spread out and includes regions occupied by clusters 5, 6 and 7 (i.e. under helix G, between helices F and G, and between helices G, H and J, respectively). MS1 is the intermediate state with the most flux during ligand binding, while the alternative binding path through MS2 (analogous to dissociation route DG from cluster 1) was observed much less, in agreement with our analysis of the RAMD simulations. Remarkably, although cluster 6 is an intermediate on the main dissociation flow (see path FGH in **Figure 2A** and the dissociation network in **Figure 3A**), it is slightly less populated and more spatially localized than cluster 7. Gating by Phe114 on the dissociation pathway is likely to be the main reason for the ligand spending time in cluster 6. However, flipping of Phe114 is rather fast and thus does not slow down ligand dissociation significantly, whereas

squeezing between helices H and J (i.e. via metastable state 7) is notably slower, making dissociation path HJ less populated.

In GaMD simulations ³², only the single intermediate state between helices D and G was reported. A similar region was assigned to an encounter state in gREST ²⁷, while an intermediate benzene position between metastable state 5 and the bound state (close to the location of cluster 4 in our study, but more spread spatially) was defined as a transient state, which again is in a qualitative agreement with our findings.

In aMD simulations ²⁵, again only two intermediate states were identified. These were denoted S2 and S3, located between helices G and H and helices F and H, respectively. S2 closely resembles the metastable state 5 in our analysis, while S3 appears similar to metastable state 6 but shifted closer to the helix H. Remarkably, the transition from S2 to S3 was found to be associated with secondary structure changes in the F- and G-helices, i.e. around Phe114, which is a key gating residue leading to the presence of metastable state 6 in our study (see next section). Since the less populated HJ egress route was not recorded in Ref. ²⁵, a state similar to cluster 7 was not observed.

Overall, the dissociation routes for benzene from T4L L99A identified in the present analysis show good qualitative agreement with the individual studies mentioned above but our analysis of the RAMD trajectories provide a more detailed and complete view of the egress pathways, including less populated pathways that were not identified in Refs. ²⁵, ³² and ²⁷.

For T4L M102A and T4L F104A, the pattern of dissociation trajectories is different from T4L L99A. Firstly, the metastable states (two for T4L M102A and one for T4L F104A, **Figure 3**) are much less populated than for T4L L99A. For T4L M102A, dissociation mainly occurs directly from cluster 5, which is very close to the bound state and resembles the position of benzene in the

highly populated metastable state 5 for T4L L99A. Benzene binds to T4L F104A in a large and open cavity and can directly dissociate without spending time in intermediate metastable states. Importantly, for both mutants, benzene has a notably smaller τ (in computations and experiments) than for T4L L99A.

In contrast, the dissociation networks for indole from T4L L99A resemble that of benzene from this mutant, with the compound passing through two intermediate metastable states along its egress route with negligible dissociation directly from the bound state. The first four clusters, however, show a larger variety of the RMSD indicating the indole position either deeper in the cavity in the vicinity of I78 of helix C (clusters 1, 2) or shifted to a more solvent-exposed region between helices D and G (clusters 3, 4). Importantly, although the flow through the metastable states 5, 7 and 8 is larger, there are many flows of significant intensity. This is in contrast to the dissociation of benzene from the T4L M104A and T4L F102A mutants, which can be described by a single predominant flow. Consistently, indole has the longest computed τ and one of the longest τ values in the experiments, comparable with that of benzene bound to T4L L99A at 10 °C.

Consideration of the dissociation rates together with the measured equilibrium dissociation rates, K_D ³⁰, shows that the mechanisms determining the length of the residence times differ among the systems studied. The difference in τ between benzene and indole for binding to T4L L99A at 20 °C can be ascribed solely to a relative stabilization of the bound state in the indole complex as both K_D and k_{off} differ by the same factor (2.3). In contrast, the difference in τ for benzene binding to T4L L99A and to T4L M102A can be ascribed solely to lowering of the transition barrier for unbinding since, at all three temperatures measured, the K_D is the same for both mutants while the k_{off} differs by a factor of 3-12. On the other hand, the difference in τ for benzene binding to the

more exposed cavity of T4L F104A versus the other mutants appears to be due to both a destabilization of the bound state and a lowering of the transition barrier. The τ RAMD method captures the trends in residence time over these systems despite the different determinants of τ . Moreover, comparison of the number of intermediate metastable states for benzene egress from the three mutants in the RAMD simulations (Figure 3A-C) is consistent with a greater number corresponding to a higher transition barrier and, therefore, a longer residence time.

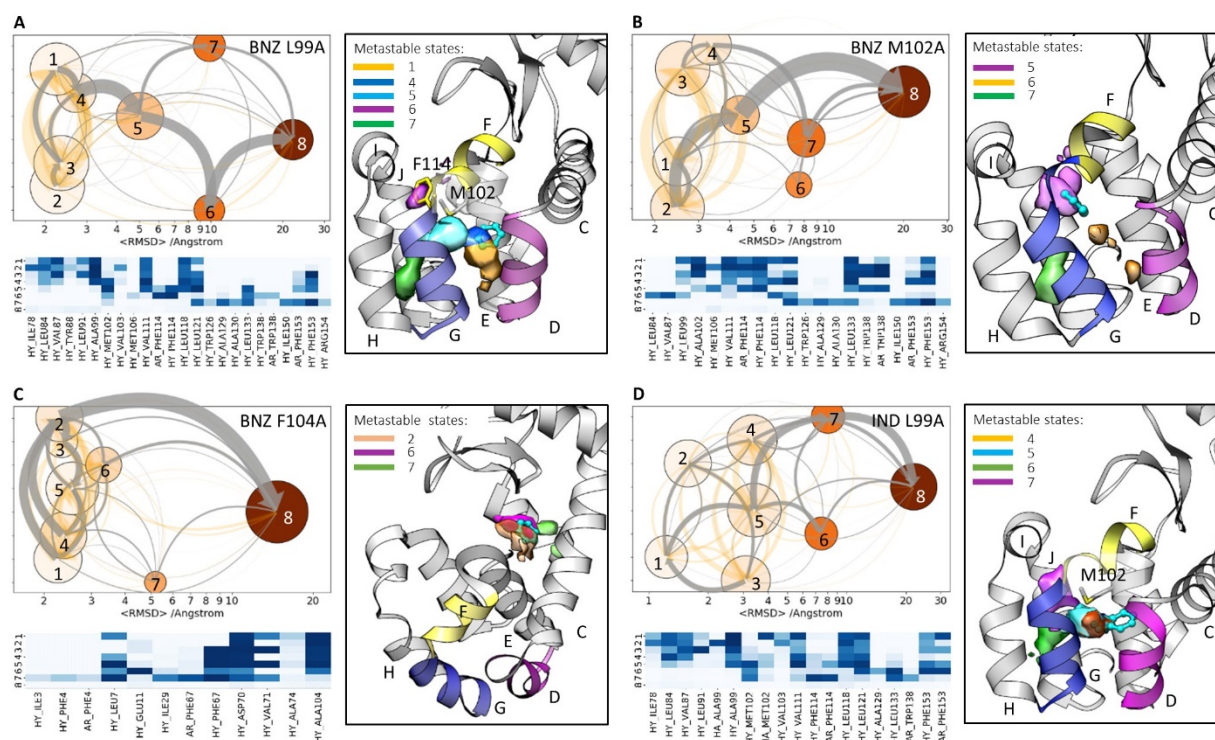


Figure 3. Analysis of benzene unbinding from T4L L99A (A), T4L M102A (B) and T4L F104A (C), and indole unbinding from T4L L99A (D) in the IFP space. Clusters were defined by clustering of frames from egress trajectories; simulations at 10 °C, 20 °C and 30 °C were clustered together. Dissociation pathways are shown in a graph-representation; each node represents a cluster or metastable state that is colored and placed according to increasing mean RMSD of the ligand in the cluster from in the starting complex; the node size denotes the cluster population; transitions between nodes are indicated by arrows for

simulations at 20 °C (transitions for simulations at 10 and 30 °C for benzene unbinding from T4L L99A are shown in **Figure S7**): the net transition flux between nodes is shown by gray arrows with their thickness proportional to the flux magnitude; the transitions between states are shown by orange arrows with their thickness proportional to the transition number. Some clusters are displayed as isosurfaces of the ligand COM population density mapped onto the 3D grid. The protein helices D, F and G are shown in pink, yellow and blue, and the ligand is shown in ball and stick representation in cyan. The heat maps show the composition of the clusters, in terms of ligand-protein contacts (color pallet from white to dark-blue indicate increasing contribution): HY: hydrophobic interactions. AR: aromatic interactions.

The role of the protein conformational flexibility and selected residues

The interactions between T4L L99A and benzene observed in the clusters can reveal residues that have important roles in unbinding, especially in clusters corresponding to intermediate states on unbinding routes, like clusters 5 and 6 (**Figure 3A**). Many residues that participate in interactions in these clusters, like Val111 and Leu133 (cluster 5) and Phe114 (cluster 6), were identified in previous computational studies as relevant for unbinding^{17,28}. Specifically, Phe114 is located at the most highly populated ligand position in cluster 6 (**Figure 3A**) leading to the predominant dissociation pathway FGH, which suggests that Phe114 necessarily flips away during ligand dissociation.

Conformational changes in T4L L99A from a highly to a lowly populated state, characterized by NMR^{34,35}, were observed to facilitate benzene unbinding through path FGH in several computational studies^{25,33}, while in other studies, such changes were observed for the binding of bulkier ligands to T4L L99A, but not for benzene²⁷. This conformational change mainly involves

helix F and one of its features is a change in the Phe114 psi angle from 50° to -40°. No clear conformational changes of the helix F backbone or of Phe114 that would characterize a transition to a lowly populated state of the protein with a conformation different from that in the bound structure were observed for benzene dissociation, although the protein RMSD as well as the dihedral angles for residues Val111-Thr115 show larger variation in RAMD dissociation simulations than in equilibration MD (**Figures S8 and S9**). The variations in protein conformation are notably greater in the case of indole dissociation, which is in line with the results of Ref. ²⁷ showing that protein distortion is caused by ligands larger than benzene.

Conclusions

We present a comprehensive computational study of the unbinding processes for complexes of T4L mutants with benzene and indole. We employed the τ RAMD method, an enhanced sampling MD approach in which an additional small force is applied to the ligand center of mass to accelerate ligand unbinding to timescales amenable to multiple MD simulations. For the systems studied, we find that, despite the nonequilibrium nature of the τ RAMD method and the general limitations of the classical force field used, it provides very good agreement between computed relative unbinding rates and experimental data obtained for distinct conditions: different complexes, different mutants and different temperatures, which can thus be directly compared and ranked. To the best of our knowledge, no other computational method has achieved this before for this or any other system.

We have furthermore found that the τ RAMD simulations augmented by MD-IFP interaction fingerprint analysis reveal details of dissociation pathways in accordance with previous much more computationally intensive studies. The metastable intermediate states identified by

τ RAMD successfully reproduce (and in some cases provide more detail than) those found by conventional MD and by other enhanced sampling methods that require at least an order of magnitude longer simulation times and much more sophisticated analysis techniques. Moreover, we found that longer τ is associated with more complex dissociation pathways with multiple intermediate metastable states (as seen for indole and benzene dissociating from T4L L99A), in contrast to the one-step dissociation observed for complexes with shorter τ (benzene – T4L M102A and T4L F104A). We also found that for benzene dissociation from T4L L99A at all three temperatures studied, there is one dominant egress path, FGH, which explains why only this pathway was found in many computational studies and indicates that accurate dissociation rates can be computed for this system even if just the main egress route is sampled.

We conclude that, despite the non-equilibrium character of the simulations, τ RAMD is able to capture the most important features determining the relative dissociation rates, while being much more computationally efficient than methods based on equilibrium MD simulations. This opens up perspectives for employing τ RAMD, in combination with the physical insights revealed here, in the rational optimization of the kinetic properties of drug candidates.

Materials and Methods

A. Molecular dynamics simulations

The structures of the complexes of benzene bound to the T4L L99A, T4L M102A and T4L F104A mutants were obtained from the PDB files 3HH4³⁶, 220L³⁷ and 227L³⁷, respectively. The crystal structure of indole bound to T4L L99A was obtained from PDB file 185L³⁸. Protonation states were assigned using pdb2pqr^{39,40} at pH 5.5 to mimic kinetic experiments³⁰. Crystallographic water molecules were maintained and crystallization molecules were removed.

The τ RAMD method¹³ was used to compute relative residence times. The protocol for the setup of each system and for molecular dynamics simulation was described in detail previously¹³ and is therefore described briefly here. The AMBER ff14SB force field⁴¹ was used for the protein and the GAFF force field⁴² for the ligand. RESP^{43,44} partial atomic charges for ligands were obtained using molecular electrostatic potentials from quantum mechanical calculations performed at the HF level with HF/6-31G** basis set using GAMESS⁴⁵. Each system was solvated in a periodic box of TIP3P water molecules with a distance of 10 Å from the solute to the box edge using tleap. 7 Na⁺ ions and 16 Cl⁻ ions were added to achieve neutrality and an approximate ionic strength of 50 mM, which mimics the conditions of the kinetic experiments. The system was energy minimized and gradually heated to 293 K in 1 ns with the Langevin thermostat and harmonic restraints of 50 kcal/(mol Å²) on all non-hydrogen atoms of the protein and the ligand using the AMBER14 software⁴⁶. Pressure was adjusted to 1 atm in a further 2 ns simulation using the Berendsen barostat. Then the system was run for 2 more nanoseconds without restraints and the final snapshot was used as input for heating and equilibration simulations carried out with the NAMD software⁴⁷. Heating from 0 to 293 K was performed for 6 ns in the NVT ensemble using

the Langevin thermostat. Then equilibration was performed for 20 ns in the NPT ensemble using the Langevin thermostat and the Nosé–Hoover barostat for temperature (293 K) and pressure (1 atm) control, respectively. Eight replicas of equilibration simulations were performed for each system. The last snapshot of each replica was used to simulate ligand dissociation. For this purpose, the RAMD method⁴⁸ was applied, in which an additional force with a magnitude of 4 kcal/(mol Å) and a random direction was applied to the center of mass (COM) of the ligand in MD simulations. Every 100 fs, the force direction was changed randomly if the ligand COM did not move further than 0.025 Å and was retained otherwise. For each of the eight equilibration replicas, 15 RAMD dissociation trajectories were generated, resulting in a total of 120 trajectories for each system. Simulations were stopped and the ligand considered to be dissociated when the distance between the COMs of the ligand and the protein was greater than 40 Å. The time required for ligand dissociation in each trajectory was stored and the recorded dissociation times for the set of trajectories were used to compute the relative residence times.

B. Analysis protocol

The protein-ligand interaction fingerprints, IFPs, were computed for the last 300 frames saved at intervals of 1 ps of each RAMD trajectory using the MD-IFP method described in ref.³¹. The IFPs analysed for benzene and indole included aromatic interactions, hydrogen bonds, and hydrophobic interactions. Additionally, the coordinates of the ligand COM and the ligand RMSD from the starting equilibrated complex were stored for each frame. The computed IFPs for the last 300 frames of each trajectory were combined in one IFP binary table for each complex (the simulations of dissociation of the benzene -T4L L99A complex at different temperatures were analysed together), with an entry of 1 if a contact was observed and zero if it was not observed. All frames were then split into 8 clusters based on their IFP composition by using a k-means

algorithm, which provided the most populated states of the ligand in the IFP space. Each cluster represents either the bound, a metastable, or the unbound state, which can be distinguished by the average RMSD of the ligand non-hydrogen atoms from their position in the starting complex. The position of the ligand COM mapped onto a 3D grid (with a spacing of 1 Å) was used to generate and display the COM density distribution for each cluster.

Additionally, the last frames of each RAMD dissociation trajectory that had IFP vectors containing at least 2 protein-ligand contacts were combined into a dissociation IFP set that was then clustered using a hierarchical clustering procedure. For each system, a variable clustering threshold was chosen in order to obtain 3-5 clusters corresponding to the main unbinding paths. The dissociation paths were then displayed by plotting the ligand COM density distribution for all trajectories or one representative trajectory in the corresponding cluster.

Supporting Information

The following files are available free of charge: Supplementary figures: analysis of benzene unbinding from T4L L99A in the IFP space using the last 500 snapshots of each RAMD trajectory (**Figure S1**); dissociation paths of indole from T4L L99A (**Figure S2**); analysis of egress routes for benzene dissociation from T4L L99A (**Figure S3**), T4L M102A (**Figure S4**) and T4L F104A (**Figure S5**); analysis of egress routes for indole dissociation from T4L L99A (**Figure S6**); analysis of benzene unbinding from T4L L99A using clustering of the last 300 frames in each trajectory in the IFP space for simulations at 10 °C and 30 °C (**Figure S7**); Ramachandran plot for several residues in the region between the F and G helices generated from the equilibration and

RAMD trajectories (**Figure S8**); RMSD plot for the non-hydrogen atoms of the residues of helix F generated from RAMD trajectories (**Figure S9**) (PDF).

AUTHOR INFORMATION

ANA, DBK and RCW conceived and planned the work. ANA and DBK performed calculations and analysis. ANA, DBK and RCW wrote the manuscript.

Notes

The authors declare no competing financial interests.

Acknowledgements This work was supported by a Capes-Humboldt postdoctoral scholarship to A N-A (Capes process number 88881.162167/2017-01), the European Union's Horizon 2020 Framework Programme for Research and Innovation under Grant Agreements 785907 and 945539 (Human Brain Project SGA2 and SGA3), and the Klaus Tschira Foundation.

REFERENCES

- 1 J. Romanowska, D. B. Kokh, J. C. Fuller and R. C. Wade, in *Thermodynamics and Kinetics of Drug Binding*, ed. (eds G. M. Keserü and D. C. Swinney), Wiley-VCH Verlag GmbH & Co. KGaA, Weinheim, Germany, Weinheim, 2015, pp. 211–235.
- 2 M. Bernetti, M. Masetti, W. Rocchia and A. Cavalli, *Annu. Rev. Phys. Chem.*, 2019, **70**, 143–171.

- 3 R. A. Copeland, *Nat. Rev. Drug Discov.*, 2016, **15**, 87–95.
- 4 D. A. Schuetz, W. E. A. de Witte, Y. C. Wong, B. Knasmueller, L. Richter, D. B. Kokh, S. K. Sadiq, R. Bosma, I. Nederpelt, L. H. Heitman, E. Segala, M. Amaral, D. Guo, D. Andres, V. Georgi, L. A. Stoddart, S. Hill, R. M. Cooke, C. De Graaf, R. Leurs, M. Frech, R. C. Wade, E. C. M. de Lange, A. P. IJzerman, A. Müller-Fahrnow and G. F. Ecker, *Drug Discov. Today*, 2017, **22**, 896–911.
- 5 N. J. Bruce, G. K. Ganotra, D. B. Kokh, S. K. Sadiq and R. C. Wade, *Curr. Opin. Struct. Biol.*, 2018, **49**, 1–10.
- 6 A. Nunes-Alves, D. B. Kokh and R. C. Wade, *Curr. Opin. Struct. Biol.*, 2020, **64**, 126–133.
- 7 D. M. Zuckerman and L. T. Chong, *Annu. Rev. Biophys.*, 2017, **46**, 43–57.
- 8 A. Laio and M. Parrinello, *Proc. Natl. Acad. Sci. U. S. A.*, 2002, **99**, 12562–6.
- 9 H. Sun, Y. Li, M. Shen, D. Li, Y. Kang and T. Hou, *J. Chem. Inf. Model.*, 2017, **57**, 1895–1906.
- 10 L. Mollica, S. Decherchi, S. R. Zia, R. Gaspari, A. Cavalli and W. Rocchia, *Sci. Rep.*, 2015, **5**, 11539.
- 11 S. Wolf, M. Amaral, M. Lowinski, F. Vallée, D. Musil, J. Güldenhaupt, M. K. Dreyer, J. Bomke, M. Frech, J. Schlitter and K. Gerwert, *J. Chem. Inf. Model.*, 2019, **59**, 5135–5147.
- 12 S. Wolf, B. Lickert, S. Bray and G. Stock, *Nat. Commun.*, 2020, **11**, 2918.
- 13 D. B. Kokh, M. Amaral, J. Bomke, U. Grädler, D. Musil, H.-P. Buchstaller, M. K. Dreyer,

- M. Frech, M. Lowinski, F. Vallee, M. Bianciotto, A. Rak and R. C. Wade, *J. Chem. Theory Comput.*, 2018, **14**, 3859–3869.
- 14 D. B. Kokh, T. Kaufmann, B. Kister and R. C. Wade, *Front. Mol. Biosci.*, 2019, **6**, 36.
- 15 A. E. Eriksson, W. A. Baase, J. A. Wozniak and B. W. Matthews, *Nature*, 1992, **355**, 371–373.
- 16 A. E. Eriksson, W. A. Baase, X. J. Zhang, D. W. Heinz, M. Blaber, E. P. Baldwin and B. W. Matthews, *Science (80-.)*, 1992, **255**, 178–183.
- 17 A. Nunes-Alves, D. M. Zuckerman and G. M. Arantes, *Biophys. J.*, 2018, **114**, 1058–1066.
- 18 Y. Wang, O. Valsson, P. Tiwary, M. Parrinello and K. Lindorff-Larsen, *J. Chem. Phys.*, 2018, **149**, 072309.
- 19 B. R. Dandekar and J. Mondal, *J Phys Chem Lett*, 2020, **11**, 5302–5311.
- 20 S. D. Lotz and A. Dickson, , DOI:10.26434/chemrxiv.12801125.v1.
- 21 P. C. T. Souza, S. Thallmair, P. Conflitti, C. Ramírez-Palacios, R. Alessandri, S. Raniolo, V. Limongelli and S. J. Marrink, *Nat. Commun.*, 2020, **11**, 3714.
- 22 R. Capelli, P. Carloni and M. Parrinello, *J. Phys. Chem. Lett.*, 2019, **10**, 3495–3499.
- 23 J. Rydzewski and O. Valsson, *J. Chem. Phys.*, 2019, **150**, 221101.
- 24 J. Rydzewski, *Comput. Phys. Commun.*, 2020, **247**, 106865.
- 25 V. A. Feher, J. M. Schiffer, D. J. Mermelstein, N. Mih, L. C. T. Pierce, J. A. McCammon

- and R. E. Amaro, *Biophys. J.*, 2019, **116**, 205–214.
- 26 J. Mondal, N. Ahalawat, S. Pandit, L. E. Kay and P. Vallurupalli, *PLOS Comput. Biol.*, 2018, **14**, e1006180.
- 27 A. Niitsu, S. Re, H. Oshima, M. Kamiya and Y. Sugita, *J. Chem. Inf. Model.*, 2019, **59**, 3879–3888.
- 28 Y. Wang, J. M. L. Ribeiro and P. Tiwary, *Nat. Commun.*, 2019, **10**, 3573.
- 29 J. M. Lamim Ribeiro and P. Tiwary, *J. Chem. Theory Comput.*, 2019, **15**, 708–719.
- 30 V. A. Feher, E. P. Baldwin and F. W. Dahlquist, *Nat. Struct. Biol.*, 1996, **3**, 516–521.
- 31 D. B. Kokh, B. Doser, S. Richter, F. Ormersbach, X. Cheng and R. C. Wade, *J. Chem. Phys.*, 2020, **153**, 125102.
- 32 Y. Miao, V. A. Feher and J. A. McCammon, *J. Chem. Theory Comput.*, 2015, **11**, 3584–3595.
- 33 Y. Wang, E. Papaleo and K. Lindorff-Larsen, *Elife*, 2016, **5**, e17505.
- 34 G. Bouvignies, P. Vallurupalli, D. F. Hansen, B. E. Correia, O. Lange, A. Bah, R. M. Vernon, F. W. Dahlquist, D. Baker and L. E. Kay, *Nature*, 2011, **477**, 111–117.
- 35 F. A. A. Mulder, A. Mittermaier, B. Hon, F. W. Dahlquist and L. E. Kay, *Nat Struct Mol Biol*, 2001, **8**, 932–935.
- 36 L. Liu, A. J. V. Marwitz, B. W. Matthews and S.-Y. Liu, *Angew. Chemie Int. Ed.*, 2009, **48**, 6817–6819.

- 37 E. Baldwin, W. A. Baase, X. Zhang, V. Feher and B. W. Matthews, *J. Mol. Biol.*, 1998, **277**, 467–485.
- 38 A. Morton and B. W. Matthews, *Biochemistry*, 1995, **34**, 8576–8588.
- 39 T. J. Dolinsky, J. E. Nielsen, J. A. McCammon and N. A. Baker, *Nucleic Acids Res.*, 2004, **32**, W665-7.
- 40 T. J. Dolinsky, P. Czodrowski, H. Li, J. E. Nielsen, J. H. Jensen, G. Klebe and N. A. Baker, *Nucleic Acids Res.*, 2007, **35**, W522–W525.
- 41 J. A. Maier, C. Martinez, K. Kasavajhala, L. Wickstrom, K. Hauser, C. Simmerling and K. E. Hauser, *J Chem Theory Comput*, 2015, **11**, 3696–3713.
- 42 J. Wang, R. M. Wolf, J. W. Caldwell, P. A. Kollman and D. A. Case, *J Comput Chem*, 2004, **25**, 1157–1174.
- 43 C. I. Bayly, P. Cieplak, W. D. Cornell and P. A. Kollman', *J. Phys. Chem*, 1993, **97**, 10269–10280.
- 44 W. D. Cornell, P. Cieplak, C. I. Bayly and P. A. Kollman, *J. Am. Chem. Soc.*, 1993, **115**, 9620–9631.
- 45 M. S. M. S. Gordon and M. W. M. W. Schmidt, *Chapter 41 – Advances in electronic structure theory: GAMESS a decade later*, Elsevier, Amsterdam, 2005.
- 46 X. W. and P. A. K. D.A. Case, V. Babin, J.T. Berryman, R.M. Betz, Q. Cai, D.S. Cerutti, T.E. Cheatham, III, T.A. Darden, R.E. Duke, H. Gohlke, A.W. Goetz, S. Gusarov, N. Homeyer, P. Janowski, J. Kaus, I. Kolossváry, A. Kovalenko, T.S. Lee, S. LeGrand, T.

- Luchko, R. Luo, B., 2014.
- 47 J. C. Phillips, R. Braun, W. Wang, J. Gumbart, E. Tajkhorshid, E. Villa, C. Chipot, R. D. Skeel, L. Kalé and K. Schulten, *J. Comput. Chem.*, 2005, **26**, 1781–1802.
- 48 S. K. Lüdemann, V. Lounnas and R. C. Wade, *J. Mol. Biol.*, 2000, **303**, 797–811.

Supplementary Information

Comprehensive characterization of ligand unbinding mechanisms and kinetics for T4 lysozyme mutants using τ RAMD

Ariane Nunes-Alves^{a,b}, Daria B. Kokh^a, Rebecca C. Wade^{a,b,c}*

^aMolecular and Cellular Modeling Group, Heidelberg Institute for Theoretical Studies, Schloss-Wolfsbrunnenweg 35, 69118 Heidelberg, Germany

^bCenter for Molecular Biology (ZMBH), DKFZ-ZMBH Alliance, Heidelberg University, Im Neuenheimer Feld 282, 69120 Heidelberg, Germany

^cInterdisciplinary Center for Scientific Computing (IWR), Heidelberg University, Im Neuenheimer Feld 205, Heidelberg, Germany.

Corresponding Author

*Rebecca.Wade@h-its.org

Supplementary Figures

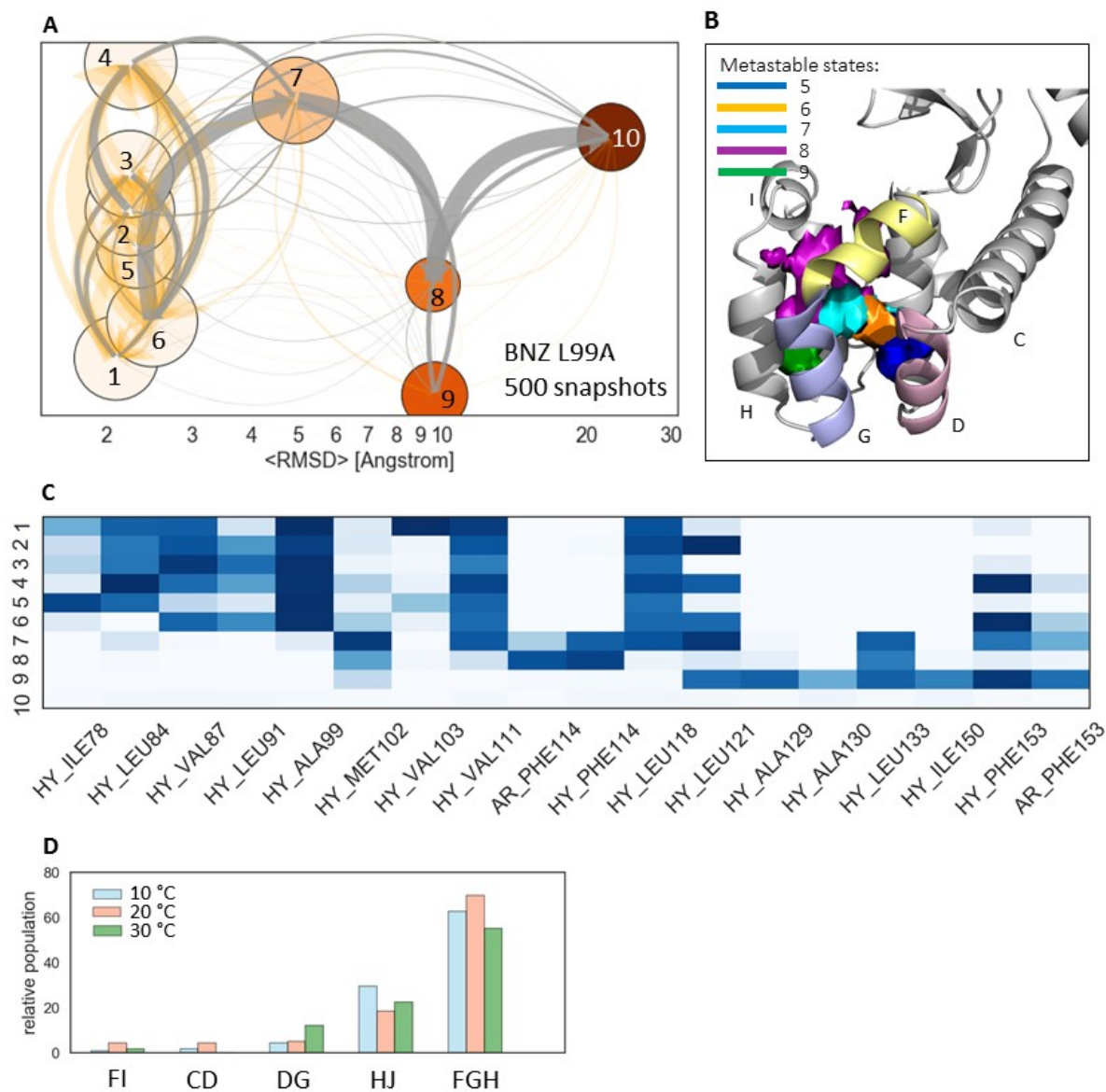


Figure S1. Analysis of benzene unbinding from T4L L99A in the IFP space using the last 500 snapshots of each RAMD trajectory. Simulations at temperatures of 10 °C, 20 °C, and 30 °C and pH 5.5 were included in the clustering procedure. (A) Dissociation pathways are shown in a graph-representation; each node represents a cluster or metastable state that is colored and placed according to increasing mean RMSD of benzene in the cluster from in the starting complex; the node size denotes the cluster population; transitions between nodes are indicated by arrows for simulations at 20 °C: the net transition flux between nodes is shown by gray arrows with thickness

proportional to the flux magnitude; transitions between states are shown by orange arrows with the thickness proportional to the transition number. (B) The clusters shown in (A) are displayed on the T4L L99A structure; selected clusters are shown by iso-surfaces of the ligand COM population density mapped onto a 3D grid; protein helices D, F and G are shown in pink, yellow and blue, and benzene is shown in ball and stick representation in cyan in its bound position. (C) Cluster composition, shown as contacts between T4L L99A and benzene and ordered by benzene RMSD. (D) Relative pathway populations observed in simulations at the three different temperatures of 10 °C, 20 °C, and 30 °C.

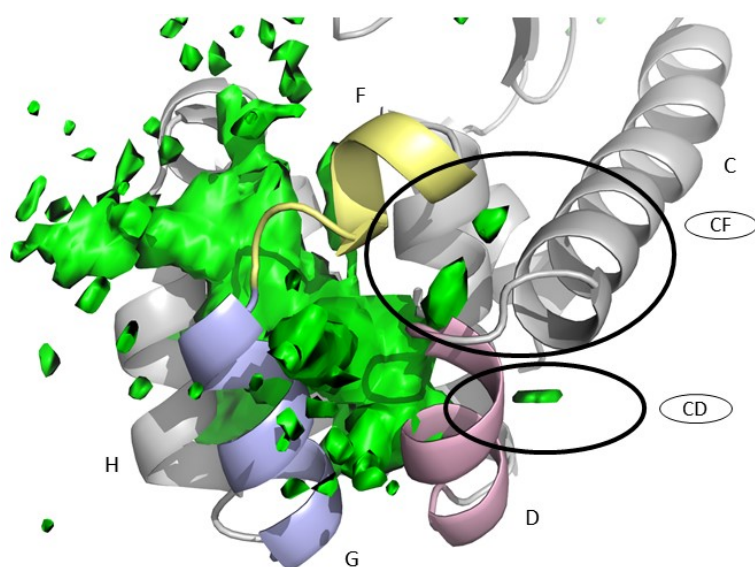


Figure S2. All dissociation paths (green) for indole from T4L L99A are displayed. Paths CD and CF have a low population ($< 5\%$) and are therefore not shown in figure 2 of the main text. The paths are represented by an isosurface of the population density obtained by mapping the positions of the ligand center of mass (COM) in all frames of the trajectories onto a 3D grid. Helices D, F and G are shown in pink, yellow and blue, respectively.

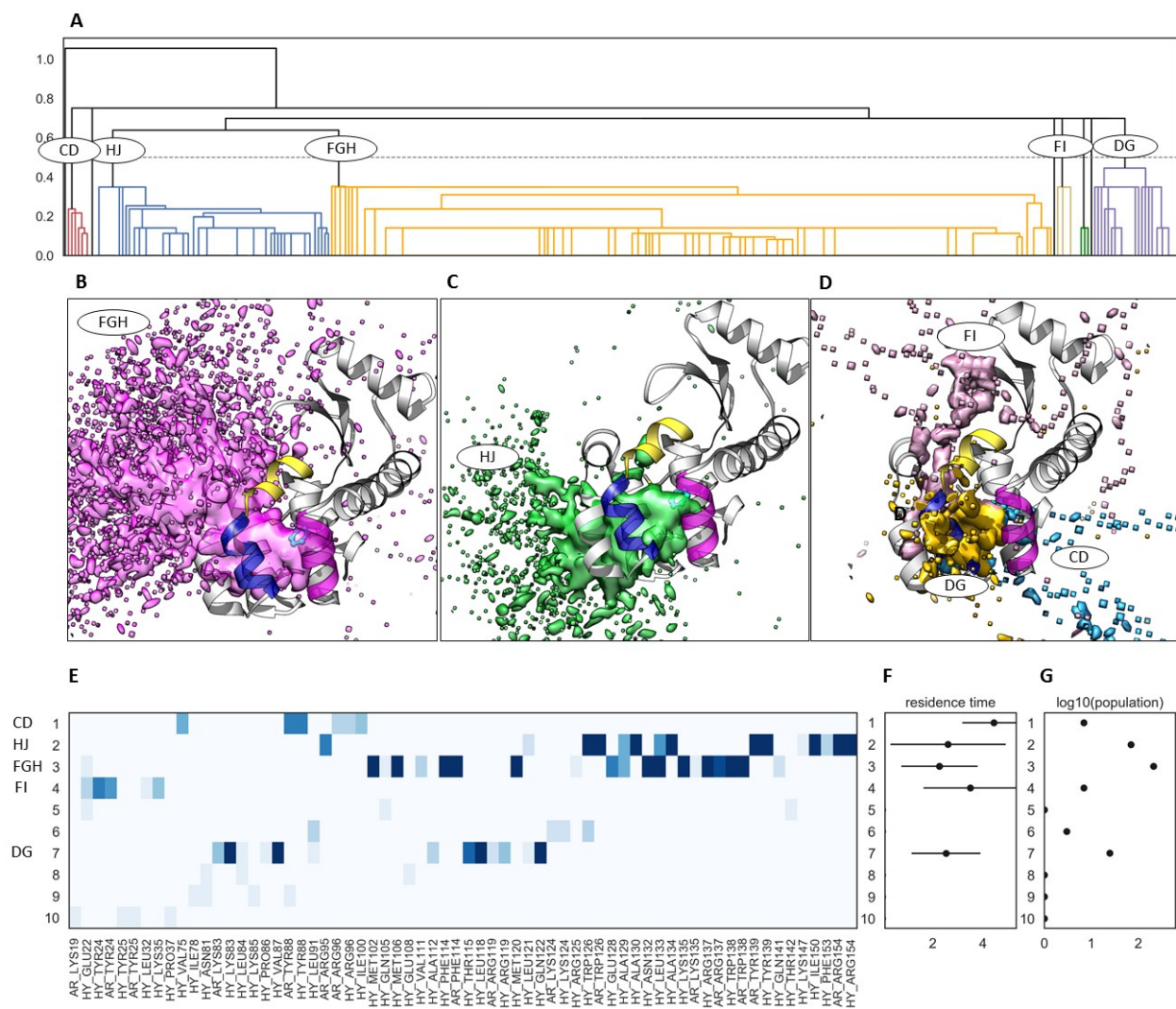


Figure S3 Analysis of egress routes for benzene dissociation from T4L L99A in RAMD simulations at three temperatures: 10 °C, 20 °C, and 30 °C. (A) Results of hierarchical clustering. (B-D) Display of the most populated clusters (populated by more than one snapshot (each representing one trajectory)). (E) Cluster composition in terms of IFPs. (F) Computed residence times (in nanoseconds) for the highly-populated clusters shown in (E). (G) The corresponding cluster populations shown on a logarithmic scale.

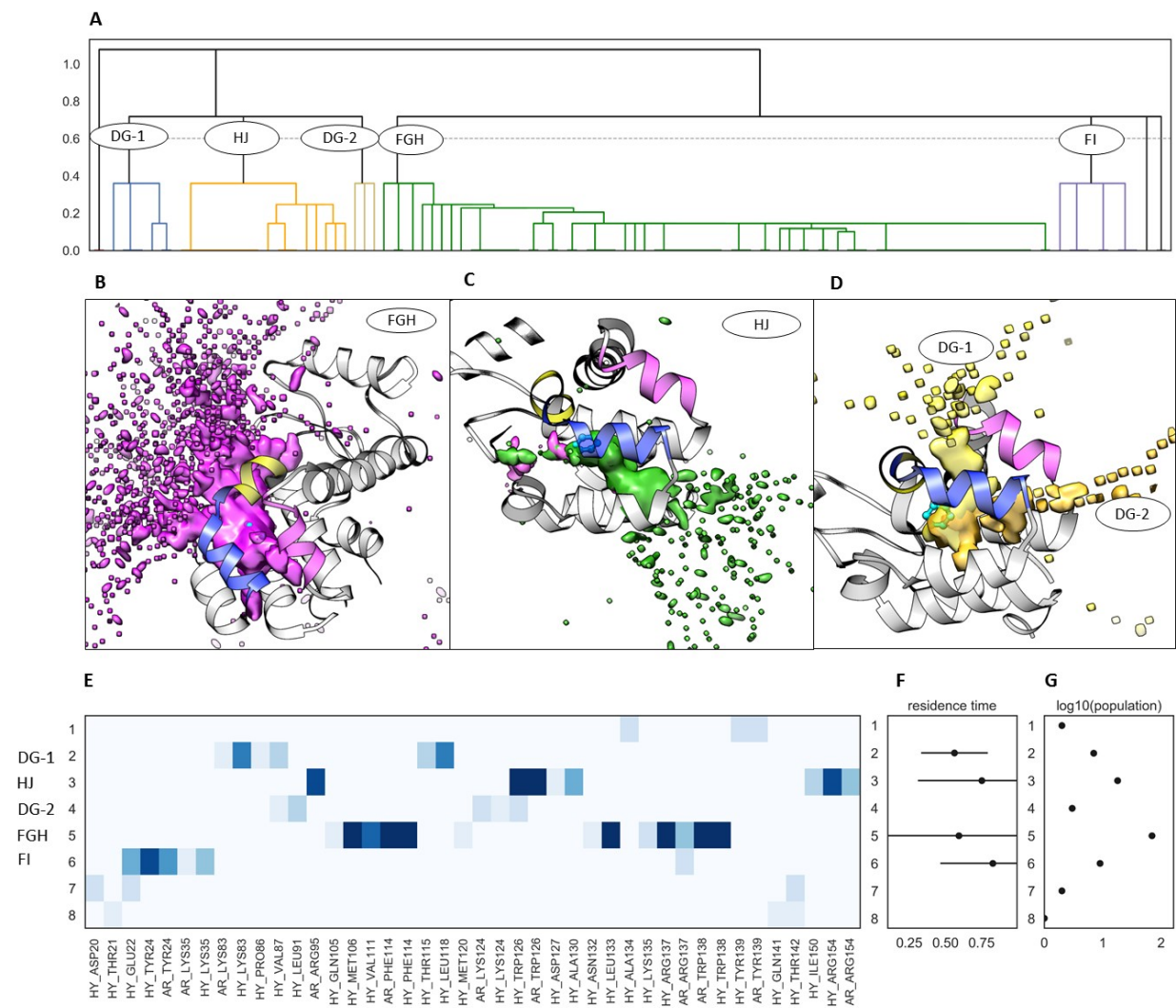


Figure S4. Analysis of egress routes for benzene dissociation from T4L M102A. Legend as for Figure S3.

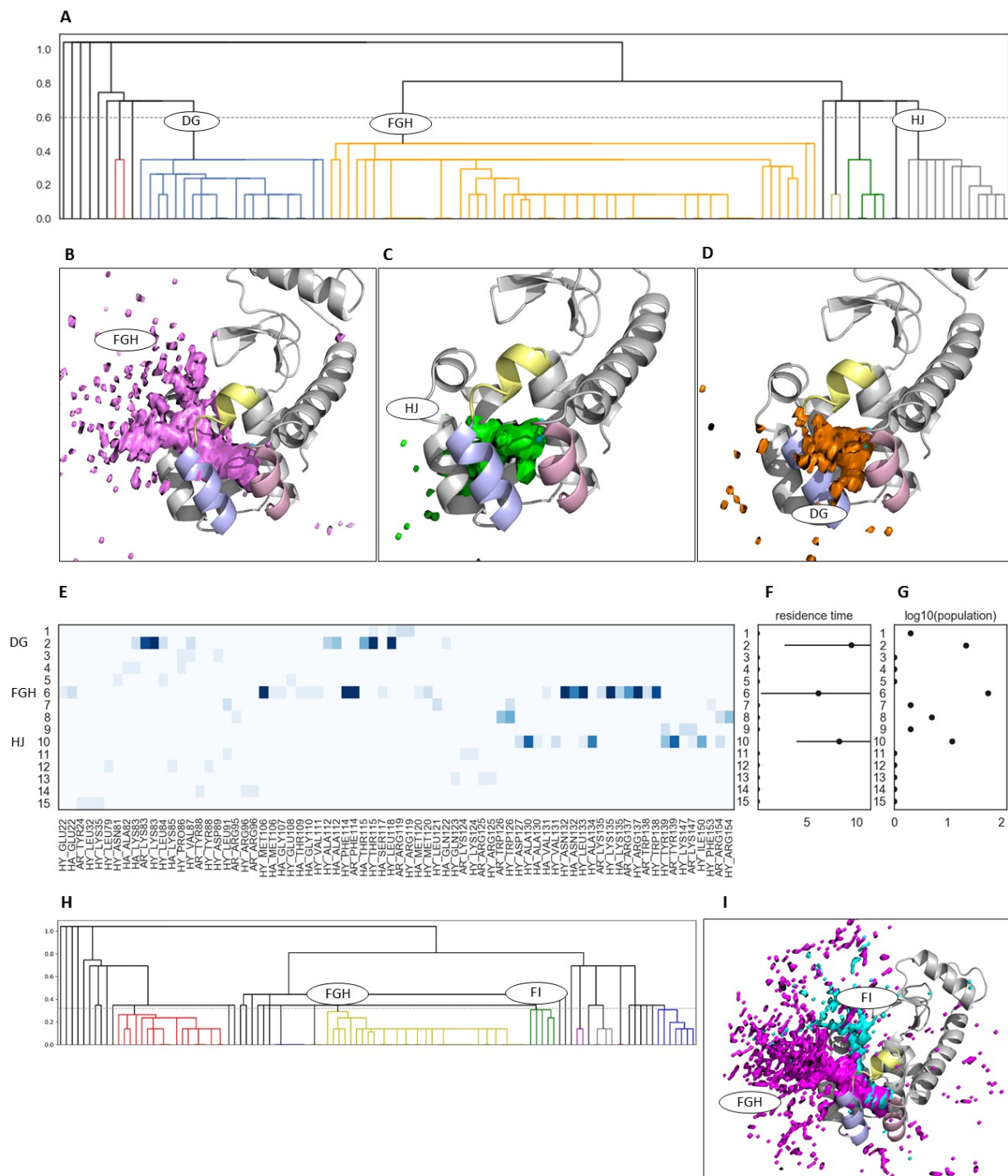


Figure S6. Analysis of egress routes for indole dissociation from T4L L99A. (A-G) Legend as for Figure S3. (H-I) Results for a smaller cutoff in the hierarchical clustering. (H) Results of hierarchical clustering. (I) Display of clusters for paths FGH and FI.

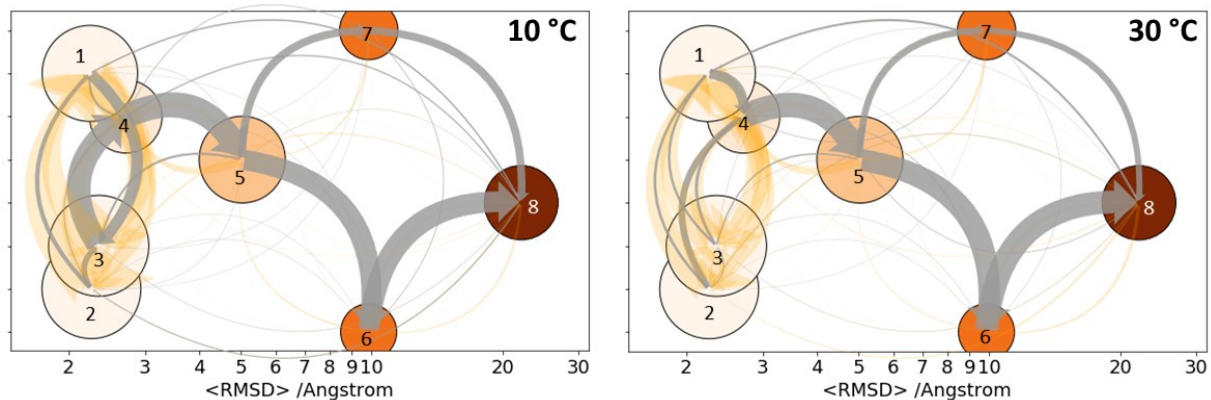


Figure S7. Analysis of egress routes for benzene from T4L L99A at 10 °C (left) and 30 °C (right). Clusters were defined by clustering of the last 300 frames in each trajectory in the IFP space; simulations at 10 °C, 20 °C and 30 °C were included in the clustering procedure. Dissociation pathways are shown in a graph representation; each node represents a cluster that is colored and positioned according to increasing mean RMSD of benzene in the cluster from in the starting complex; the node size denotes the cluster population; transitions between nodes are indicated by arrows for simulations: the net transition flux between nodes is shown by gray arrows with their thickness proportional to the flux magnitude; transition between states are shown by orange arrows with their thickness proportional to the transition number.

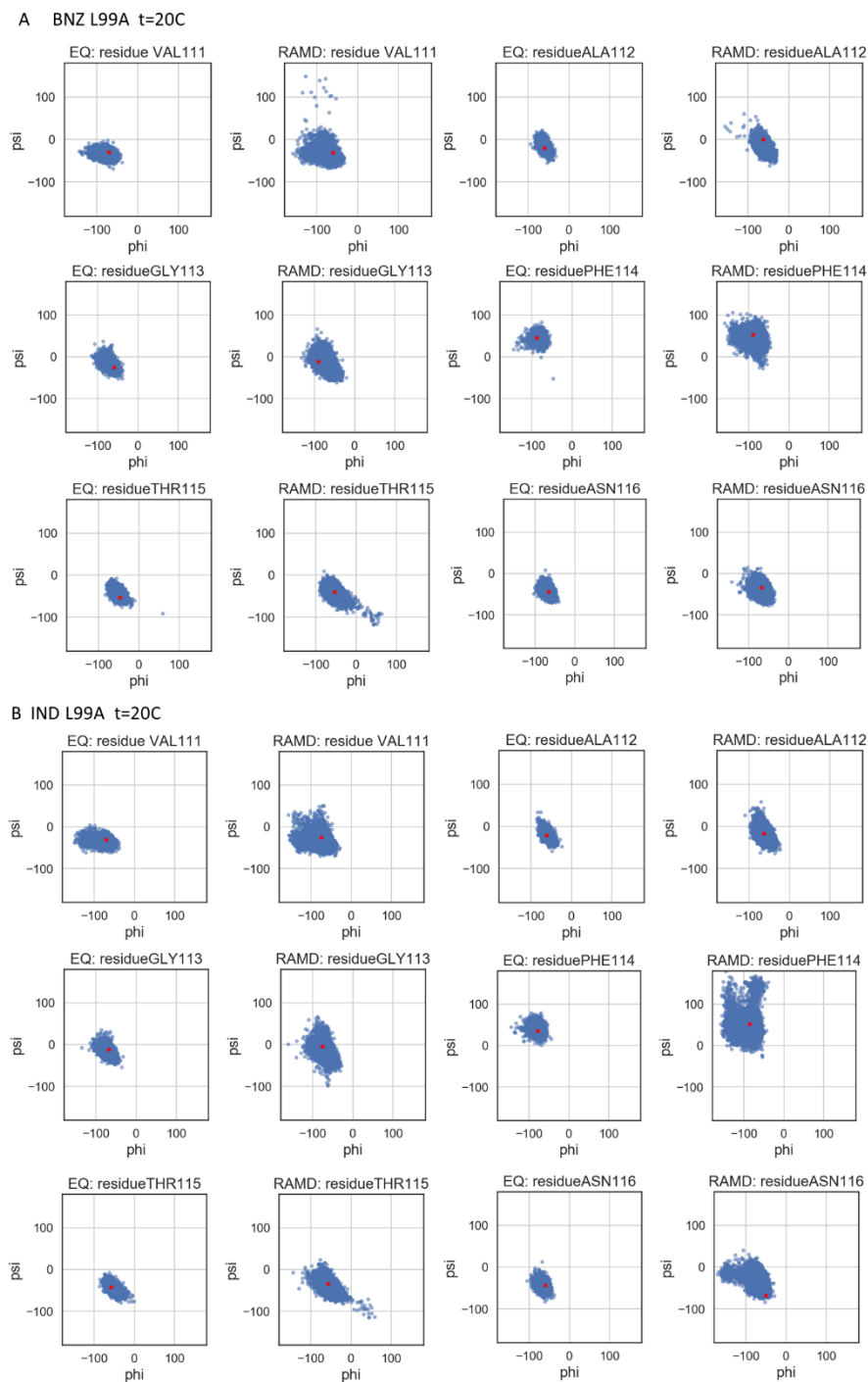


Figure S8. Ramachandran plots for several residues in the region between the F and G helices generated from the equilibration (EQ) and RAMD trajectories (the last 300 snapshots from each trajectory were used in the analysis) of T4L L99A for the egress of (A) benzene and (B) indole at 20 °C. The red dots show the angles for the corresponding crystal structures.

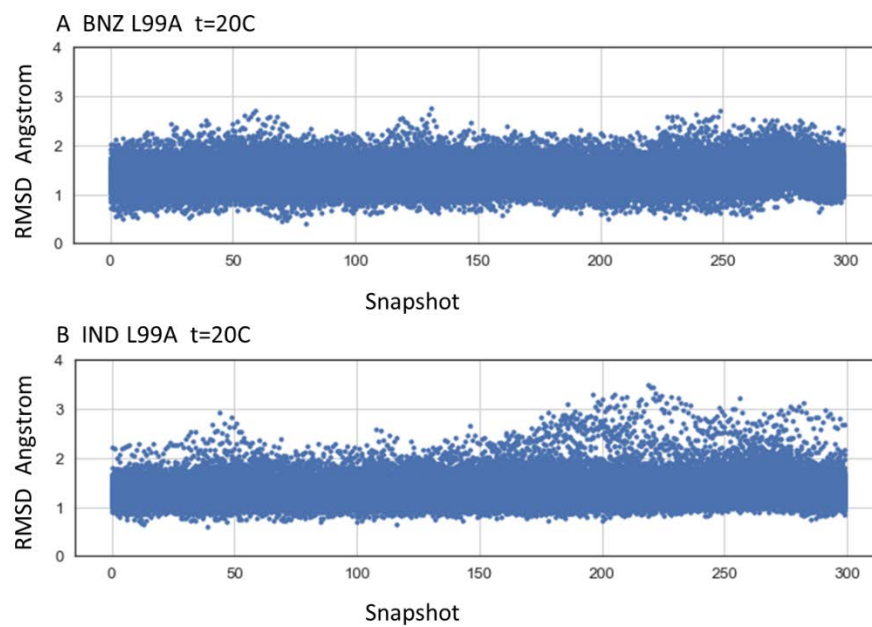


Figure S9. RMSD of the non-hydrogen atoms of the residues of helix F (G108 – T115) relative to the starting structure of the T4L L99A – ligand complex, plotted for the last 300 snapshots of each RAMD trajectory for (A) benzene and (B) indole dissociating from T4L L99A at 20 °C.